



**HAL**  
open science

## Electronic structure, low-temperature transport and thermodynamic properties of polymorphic $\beta$ -As<sub>2</sub>Te<sub>3</sub>

Jean-Baptiste Vaney, Jean-Claude Crivello, Cédric Morin, Gaëlle Delaizir, Julie Carreaud, Andrea Piarristeguy, Judith Monnier, Eric Alleno, Annie Pradel, Elsa B. Lopes, et al.

► **To cite this version:**

Jean-Baptiste Vaney, Jean-Claude Crivello, Cédric Morin, Gaëlle Delaizir, Julie Carreaud, et al.. Electronic structure, low-temperature transport and thermodynamic properties of polymorphic  $\beta$ -As<sub>2</sub>Te<sub>3</sub>. RSC Advances, 2016, 6 (57), pp.52048-52057. 10.1039/c6ra01770c . hal-01325342

**HAL Id: hal-01325342**

**<https://hal.science/hal-01325342>**

Submitted on 15 Oct 2020

**HAL** is a multi-disciplinary open access archive for the deposit and dissemination of scientific research documents, whether they are published or not. The documents may come from teaching and research institutions in France or abroad, or from public or private research centers.

L'archive ouverte pluridisciplinaire **HAL**, est destinée au dépôt et à la diffusion de documents scientifiques de niveau recherche, publiés ou non, émanant des établissements d'enseignement et de recherche français ou étrangers, des laboratoires publics ou privés.



CrossMark  
click for updates

Cite this: *RSC Adv.*, 2016, 6, 52048

# Electronic structure, low-temperature transport and thermodynamic properties of polymorphic $\beta$ -As<sub>2</sub>Te<sub>3</sub>†

J.-B. Vaney,<sup>a</sup> J.-C. Crivello,<sup>b</sup> C. Morin,<sup>b</sup> G. Delaizir,<sup>c</sup> J. Carreaud,<sup>c</sup> A. Piarristeguy,<sup>d</sup> J. Monnier,<sup>b</sup> E. Alleno,<sup>b</sup> A. Pradel,<sup>d</sup> E. B. Lopes,<sup>e</sup> A. P. Gonçalves,<sup>e</sup> A. Dauscher,<sup>a</sup> C. Candolfi<sup>a</sup> and B. Lenoir<sup>\*a</sup>

$\beta$ -As<sub>2</sub>Te<sub>3</sub> belongs to the prominent family of Bi<sub>2</sub>Te<sub>3</sub>-based materials, which show excellent thermoelectric properties near room temperature. In this study, we report a joint theoretical and experimental investigation of its electronic and thermal properties at low temperatures (5–300 K). These results are complemented by specific heat measurements (1.8–300 K) that provide further experimental evidence of the first order lattice distortion undergone by  $\beta$ -As<sub>2</sub>Te<sub>3</sub> near 190 K. Data taken on cooling and heating across this transition show that the lattice distortion has little influence on the electronic properties and further evidence a weak hysteretic behavior. Although first-principles calculations predict a semiconducting ground state, these measurements show that  $\beta$ -As<sub>2</sub>Te<sub>3</sub> behaves as a degenerate p-type semiconductor with a high carrier concentration of 10<sup>20</sup> cm<sup>-3</sup> at 300 K likely due to intrinsic defects. Calculations of the vibrational properties indicate that the extremely low lattice thermal conductivity values (0.8 W m<sup>-1</sup> K<sup>-1</sup> at 300 K) mainly originate from low-energy Te optical modes that limit the energy window of the acoustic branches. This limited ability to transport heat combined with a relatively large band gap suggest that high thermoelectric efficiency could be achieved in this compound when appropriately doped.

Received 20th January 2016  
Accepted 20th May 2016

DOI: 10.1039/c6ra01770c

www.rsc.org/advances

## Introduction

Thermoelectric materials, that directly convert either heat into electricity or electricity into a thermal gradient, are used in solid-state devices that enable waste-heat harvesting or powering of deep space probes and rovers.<sup>1,2</sup> The efficiency of a thermoelectric device, should it be used as a generator or solid-state cooler, is governed by the dimensionless figure of merit  $ZT$  defined at the operating temperature  $T$  as  $ZT = \alpha^2 T / \rho(\kappa_e + \kappa_L)$ .<sup>1</sup> High thermoelectric performances require the design of high- $ZT$  materials in which a fine balance between the thermopower  $\alpha$ , the electrical resistivity  $\rho$  and the electronic and lattice thermal conductivities  $\kappa_e$  and  $\kappa_L$ , respectively, must be achieved. Among frequently used strategies for optimizing the thermoelectric properties, the search for materials that are poor thermal conductors proved to be a fruitful way of research. This

approach led to the identification of many families of compounds, such as Zintl phases,<sup>3–7</sup> cluster compounds,<sup>8–10</sup> chalcogenides,<sup>11–16</sup> or natural minerals,<sup>17–22</sup> that all exhibit the desirable features of good thermoelectric materials: a complex crystal structure to limit the heat conduction combined with semiconducting-like electronic properties that can be engineered through doping.

Despite strong efforts devoted to the search for materials able to operate at ambient temperature, the semiconducting (Bi,Sb)<sub>2</sub>X<sub>3</sub>-based alloys (X = Se, Te) still remain to date the most prominent class of thermoelectric materials for room-temperature thermoelectric applications.<sup>1,2</sup> These compounds crystallize in a rhombohedral unit cell leading to isotropic transport properties in both single-crystalline and in some polycrystalline samples depending on the synthesis process. A large number of substituting elements can be used to alter their transport properties resulting in a wide variety of physical phenomena,<sup>23,24</sup> in addition to their Dirac-like conducting surface states classifying these compounds as 3D topological insulators.<sup>25–27</sup>

Recently, our initial investigation on the high-temperature thermoelectric properties of a new member of this family, namely  $\beta$ -As<sub>2</sub>Te<sub>3</sub>, evidenced extremely low lattice thermal conductivity approaching the amorphous limit (0.5 W m<sup>-1</sup> K<sup>-1</sup> at 423 K).<sup>28</sup> This property, combined with enhanced power factors due to Sn doping, resulted in a peak  $ZT$  of 0.65 at 423 K.

<sup>a</sup>Institut Jean Lamour, UMR 7198 CNRS – Université de Lorraine, Nancy, France. E-mail: bertrand.lenoir@univ-lorraine.fr

<sup>b</sup>Institut de Chimie et des Matériaux Paris Est (ICMPE), UMR 7182 CNRS-Université Paris-Est Créteil, Thiais, France

<sup>c</sup>Science des Procédés Céramiques et de Traitements de Surface (SPCTS), UMR CNRS 7315-Université de Limoges, France

<sup>d</sup>Institut Charles Gerhardt (ICG), UMR 5253 CNRS-Université de Montpellier, France

<sup>e</sup>C2TN, Instituto Superior Técnico, Universidade de Lisboa, Lisboa, Portugal

† Electronic supplementary information (ESI) available. See DOI: 10.1039/c6ra01770c

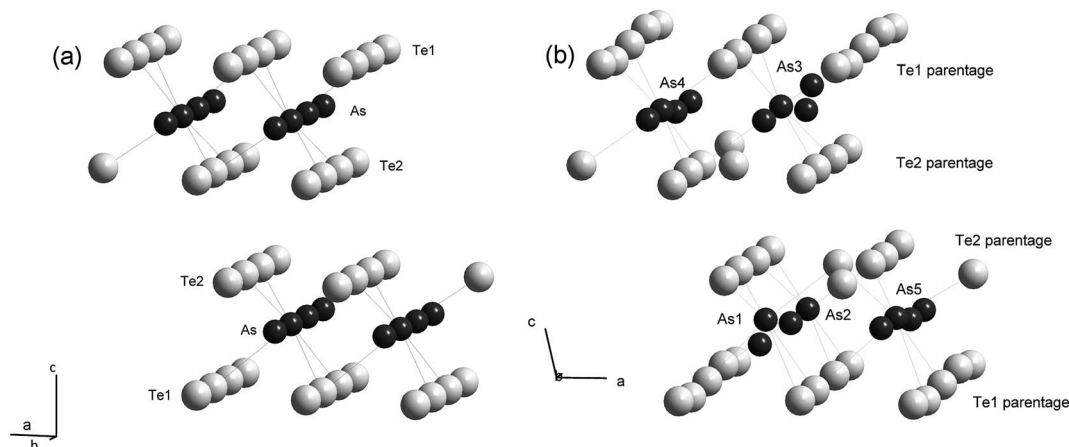


Fig. 1 Comparison of the rhombohedral ( $R\bar{3}m$ ) crystal structure (panel a) and the monoclinic ( $P2_1/m$ ) crystal structure (panel b) of the  $\beta$  and  $\beta'$  phases, respectively. Besides a slight distortion of the unit cell, a fourfold modulation of the atomic positions longitudinal and transverse to the  $b$  axis is observed in the  $\beta'$  phase. Both structures were drawn by using the experimental data obtained in ref. 29.

Further, joint laboratory X-ray and neutron diffraction experiments carried out on  $\beta$ - $\text{As}_2\text{Te}_3$  revealed a reversible first-order phase transition to a distorted monoclinic phase (space group  $P2_1/m$ ) upon cooling below 210 K.<sup>29</sup> Another consequence of this subtle structural transition from the  $\beta$  phase to the new  $\beta'$  phase is a fourfold modulation of the atomic positions along the  $b$  axis (Fig. 1). This structural instability was backed up by first-principles calculations of the formation energies indicating that the  $\beta'$  phase is more stable than the  $\beta$  polymorph at 0 K.<sup>29</sup> Yet, the low-temperature physical properties of  $\beta$ - $\text{As}_2\text{Te}_3$  as well as the influence of the lattice distortion on the transport remain so far unexplored.

Herein, we provide a detailed investigation of the transport and thermodynamic properties of  $\beta$ - $\text{As}_2\text{Te}_3$  below 300 K. Because first-principle calculations are essential for modeling the transport and for guiding future efforts to improve the thermoelectric properties of this material, our experimental findings are complemented by calculations of the electronic and phonon densities of states and dispersion curves of both the  $\beta$  and  $\beta'$  phases, which are discussed in light of prior theoretical studies carried out on  $\beta$ - $\text{As}_2\text{Te}_3$ .

## Experimental and computational details

### Electronic band structure and phonon calculations

Density functional theory (DFT) calculations were performed using the projector augmented wave method (PAW),<sup>30</sup> implemented in the Vienna *Ab initio* Simulation Package (VASP) code under the generalized gradient approximation (GGA) using the Perdew–Burke–Ernzerhof (PBE) exchange–correlation functional.<sup>31–33</sup> A dense grid of  $k$ -points in the irreducible wedge of the Brillouin zone was considered together with cut-off energy for the pseudo-potentials set to 800 eV. The electronic densities of states (DOS) were obtained using the linear tetrahedron method with Blöchl corrections done on the relaxed structures.<sup>30</sup> The results of the relaxed crystallographic parameters

and heat of formation of the polymorphic  $\text{As}_2\text{Te}_3$  phases were already discussed in our prior study.<sup>29</sup> The results indicated that the  $\alpha$ -phase is the most stable structure, while the  $\beta'$ -phase was predicted to be more stable than the  $\beta$ -phase, in agreement with our experimental findings. For sake of completeness, we present the calculations performed on the  $\alpha$ -phase in the ESI file.†

Phonon calculations were performed by a supercell approach with the finite displacement method within both the harmonic (HA) and quasi-harmonic approximation (QHA) using the Phonopy code.<sup>34–36</sup> Details concerning the unit cells containing from 60 to 80 atoms, which have been considered, are summarized in Table 1.

### Synthesis, structural and chemical characterizations

$\beta$ - $\text{As}_2\text{Te}_3$  was synthesized by direct melting of stoichiometric quantities of high purity elements (99.99% As and 99.999% Te) in powder form in sealed evacuated quartz tubes.<sup>28,29</sup> Prior to use, elemental As powder was purified in sealed quartz tubes at 558 K for 2 h in order to eliminate oxide traces. The tube was heated at 923 K at 10 K h<sup>−1</sup>, held at this temperature for 2 h and finally quenched in room-temperature water. The resulting ingot was ground into fine powders, which were subsequently consolidated at room temperature under 750 MPa of pressure. Crystal structure and phase purity were verified by powder X-ray diffraction (PXRD) and scanning electron microscopy (SEM). Both experiments confirmed the successful synthesis of a phase-pure sample of  $\beta$ - $\text{As}_2\text{Te}_3$  (Fig. S1 in ESI†). The room-temperature lattice parameters are  $a = 4.0463(5)$  Å and  $c = 29.505(3)$  Å, in good agreement with those determined in ref. 29.

### Transport and thermodynamic properties measurements

Low-temperature electrical resistivity, thermopower and thermal conductivity were measured simultaneously using the thermal transport option of a physical property measurement system (PPMS, Quantum Design) upon cooling (300–5 K) and heating (5–300 K). To probe the anisotropy in the transport

**Table 1** Crystallographic parameters, electronic band gap, phonon supercell details and heats of formation (gross and ZPE corrected) of the polymorphic As<sub>2</sub>Te<sub>3</sub> phases obtained after the full DFT relaxation. For sake of completeness, the parameters of the  $\alpha$  phase are also added. The experimental data obtained at 300 K on the  $\alpha$  and  $\beta$  phase in ref. 29 are mentioned in parenthesis. The crystallographic data of the  $\beta'$  phase (ref. 29) were determined at 20 K. When available, the experimental band gap is also mentioned

	$\alpha$ C2/m (12)	$\beta$ R $\bar{3}m$ (166)	$\beta'$ P2 <sub>1</sub> /m (11)	$\beta'$ C2/m (12)
$a$ (Å)	14.962 (14.337)	4.102 (4.047)	7.087 (6.99)	7.088
$b$ (Å)	4.071 (4.015)	—	16.366 (16.24)	4.092
$c$ (Å)	10.130 (9.887)	29.745 (29.498)	10.475 (10.25)	10.463
$\beta$ (°)	95.579 (95.06)	—	103.016 (103.4)	103.044
Volume (Å <sup>3</sup> atom <sup>-1</sup> )	30.701 (28.456)	28.893 (27.893)	29.592 (28.297)	29.560
Theoretical band gap (eV)	0.46	0.30	0.39	0.39
Experimental band gap (eV)	0.43 (ref. 42)	—	—	—
Phonon supercell	2 × 2 × 2 (80 at)	2 × 2 × 1 (60 at)	1 × 1 × 1 (80 at)	2 × 2 × 2 (80 at)

properties, bar-shaped samples of well-defined geometry ( $\sim 2.5 \times 3 \times 8$  mm<sup>3</sup>) were cut in the consolidated ingots both parallel and perpendicular to the pressing direction with a diamond-wire saw. To ensure good electrical and thermal contacts, four copper tabs were soldered with a low melting point braze. The temperature gradient was established by applying heat at one end of the specimen while holding the other end at a constant temperature by maintaining a good thermal contact to a heat sink. Calibrated cernox thermometers were attached to the sample between 2.5 and 3.5 mm apart. The temperature difference was monitored to amount to 2% of the temperature at which the measurement was done. The voltage and temperature difference were measured at the same positions along the sample. The data collected were corrected for thermal radiations by a model implemented in the TTO option software by Quantum Design that uses an accurate estimate of the bath temperature around the sample.

The Hall resistivity was determined from measurements of the transverse electrical resistivity  $\rho_{xy}$  under magnetic fields  $\mu_0 H$  ranging between  $-1$  and  $+1$  T. The data were corrected for slight misalignment of the contacts by applying the formula  $\rho_H = [\rho_{xy}(\mu_0 H) - \rho_{xy}(-\mu_0 H)]/2$ . The Hall coefficient  $R_H$  was determined from the slope of the  $\rho_H(\mu_0 H)$  data in the limit  $\mu_0 H \rightarrow 0$ . The Hall carrier concentration  $p$  and mobility  $\mu_H$  were estimated within a single-band model with a Hall factor  $r_H$  equal to 1 that yields the relations  $p = r_H/R_H e = 1/R_H e$  and  $\mu_H = R_H/\rho$ . Specific heat measurements were carried out on cooling and heating between 1.8 and 300 K using the dedicated option of the PPMS. A sample of approximately 20 mg was glued on the sample holder with a tiny amount of Apiezon N grease. The experimental uncertainty on the transport, Hall effect and specific heat measurements is estimated to be 5%, 5% and 3%, respectively.

## Results and discussion

### Electronic band structure

Fig. 2a shows the electronic band structure and the integrated density of states (DOS) of the  $\beta'$ -As<sub>2</sub>Te<sub>3</sub> phase calculated in the P2<sub>1</sub>/m symmetry. Because of the strong similarities between the crystal structure of the  $\beta'$  and  $\beta$  phases, the electronic properties are very similar. The electronic structure of the  $\beta$  polymorph, in

agreement with those reported in prior studies, shares similarities with that of Bi<sub>2</sub>Te<sub>3</sub>, notably the presence of six-fold degenerate band edges.<sup>37</sup> In the  $\beta'$  phase, the low-energy dispersive bands located between  $-13.5$  and  $-7.5$  eV below the Fermi level originates from the interaction between the non-localized 4s-As and the 5s-Te states. Compared to  $\beta$ -As<sub>2</sub>Te<sub>3</sub>, this structure is less broad owing to a stronger localization of s-electrons due to the reduced unit cell volume of the  $\beta'$  phase. The region between the bonding and anti-bonding 4s-As states is highly dense and corresponds to localized bands of 5s-Te states that lead to high peaks in the partial DOS (Fig. 2b and S4 in ESI†).

The valence bands, extending over  $\sim 5.5$  eV, are separated from this region by a gap of about 2 eV. The valence bands are flat and mainly dominated by the 4p-As and the 5p-Te states. As shown in the magnified Fig. 2c, the valence band maximum and conduction band minimum are located along the D–E direction resulting in a slightly indirect band gap of 0.39 eV ( $\Delta k = 0.05 \times 2\pi a^*$  where  $a^*$  is the reciprocal lattice vector). The directional effective mass of holes along the D–E direction  $m_{D-E}^*$  is estimated to  $0.31m_0$  where  $m_0$  is the free electron mass. The Fermi level has been conventionally set at the top of the valence bands. The magnitude of the band gap in the  $\beta'$  phase is slightly higher than that obtained in the  $\beta$  phase which features a direct band gap of 0.30 eV (Fig. S6 and S8 in ESI†). This value is higher than that calculated in ref. 38 where a direct band gap of 0.24 eV was found at the  $\Gamma$  point. A comparison of these findings with the literature indicates a rather large discrepancy among the results reported for the  $\beta$  phase. While our value agrees with that obtained by Pal *et al.*<sup>39</sup> who found a band gap of 0.35 eV with calculation based on all-electron full potential linearized augmented plane wave (FP-LAPW) technique, prior values derived theoretically (0.12 eV in ref. 37 and 0.22 eV in ref. 40) are significantly lower. These differences in the computed band gaps are most likely due to the different methodologies used, both the direct or indirect nature of the band gap and its value being strongly sensitive to details of the calculations.

In the prior study of Pal *et al.*,<sup>39</sup> a compressive strain applied along the  $c$ -axis of the crystal structure was used to predict the transition from a trivial band insulator to a topological insulating state in  $\beta$ -As<sub>2</sub>Te<sub>3</sub>. Following this approach, we compared the evolution of the band gap under an isotropic stress for

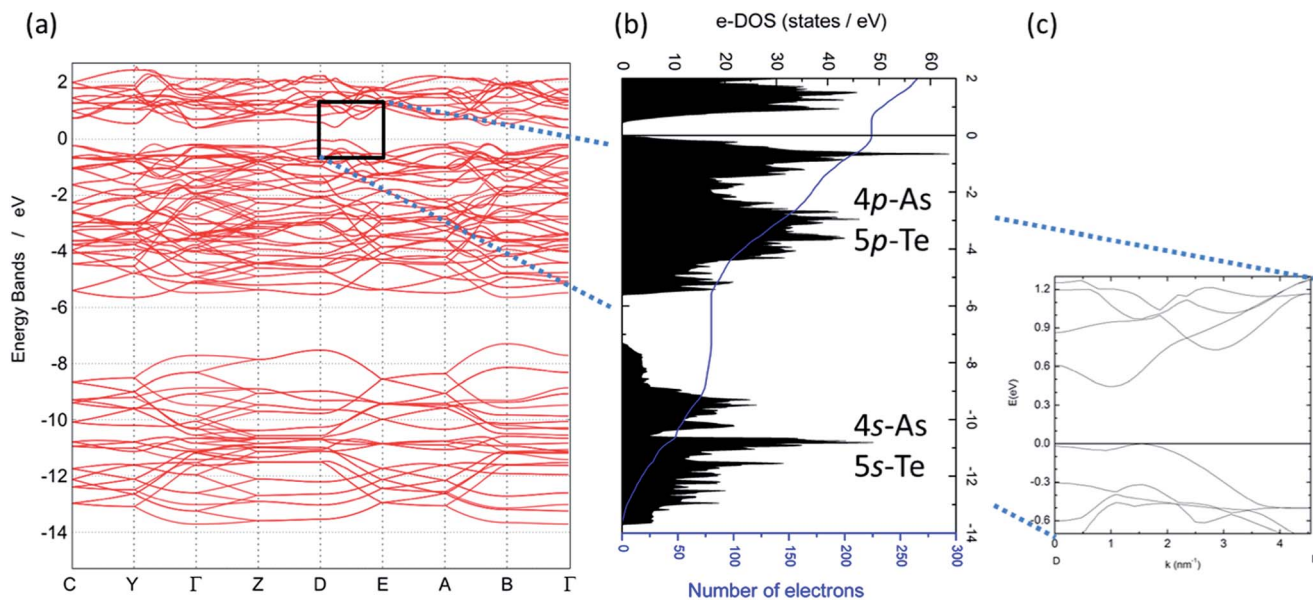


Fig. 2 Electronic structure of the  $\beta'$ -As<sub>2</sub>Te<sub>3</sub> phase: (a) dispersion curves along high symmetry directions represented in the irreducible  $P2_1/m$  Brillouin zone and (b) density of states (DOS) as a function of the energy. The Fermi level has been chosen as the origin of energies. (c) Magnification of the dispersion curves around the electronic band gap showing the four-top valence bands and the four top-most conduction bands.

$\beta$ -As<sub>2</sub>Te<sub>3</sub> and  $\beta'$ -As<sub>2</sub>Te<sub>3</sub> (Fig. S16 and S17 in ESI†). For both phases, the uniaxial compression leads to the inversion of the top of the valence band and the bottom of the conduction band at  $\Delta V/V \sim -7\%$ , accompanied by a metallic state transition. This band inversion and parity reversal of bulk electronic bands are characteristic of an electronic topological phase transition. Although the isotropic stress shows some deviations compared to the uniaxial strain (inversion at  $\Delta V/V \sim -5\%$  in ref. 39), our results demonstrate a similar behavior of the  $\beta$  and  $\beta'$  phases. Hence, the lattice distortion does not preclude the observation of a topological state under pressure in this compound.

### Phonon dispersion curves

The detailed results about the vibrational properties of the pure elements and of the different polymorphic phases of As<sub>2</sub>Te<sub>3</sub> calculated within the harmonic approximation are given in the ESI.† Phonon dispersion curves, integrated partial DOS of atoms in equivalent sites and thermodynamic properties are provided for the pure elements (As, Te) in their stable reference state, and for the polymorphic As<sub>2</sub>Te<sub>3</sub> considering three crystallographic structures: the  $\beta$ -phase (space group  $R3m$ ) and the  $\beta'$ -phase described either in the space groups  $P2_1/m$  or  $C2/m$ .

The phonon dispersion curves and the partial phonon DOS (PDOS) of  $\beta'$ -As<sub>2</sub>Te<sub>3</sub> calculated in space group  $C2/m$  are depicted in Fig. 3a. Because of the mass ratio between As and Te, the top of the optical branches of As is located at higher frequencies (6.0 THz) with respect to that of the Te atoms (4.2 THz). The phonon dispersion curves of the three polymorphic As<sub>2</sub>Te<sub>3</sub> phases exhibit fairly soft modes since the highest frequencies do not exceed 6.0 THz ( $\sim 200 \text{ cm}^{-1}$  or  $\sim 25 \text{ meV}$ , see Fig. S12 to S15 in ESI†). Due to the mass ratio, the center of gravity of the PDOS of

Te appears at lower frequencies compared to As, regardless of the investigated structures. As shown in Fig. 3b, the PDOS of Te can be decomposed into the 2a and 4i contributions. The Te atoms in the 2a site (Te<sub>1</sub>) contribute mainly at energies above 3 THz where the observed large PDOS corresponds to interactions with the 6 neighboring As atoms at about 3.0 Å. According to the coordination environment, the PDOS of Te in the 4i site (Te<sub>2</sub>) exhibits two main structures: one centered at low energies around 2.1 THz which corresponds to the interaction with three other Te<sub>2</sub> atoms on the same site at  $\sim 3.6 \text{ Å}$ , *i.e.* across the van der Waals interspace, and another peak at higher frequencies (above 2.6 THz) corresponding to the interaction with the closest As atoms ( $\sim 2.8 \text{ Å}$ ). The acoustic phonon bands are limited to very low energies suggesting a poor ability of the  $\beta'$  phase to conduct heat. This result is consistent with the very low thermal conductivity values of the  $\beta$  phase measured above 300 K (ref. 28) and, as we shall see below, with the measurements at low temperatures.

The phonon dispersion curves of  $\beta'$ -As<sub>2</sub>Te<sub>3</sub> calculated in the  $P2_1/m$  space group feature negative frequencies (see Fig. S15 in ESI†), while those calculated in the space group  $C2/m$  are only positive. This important difference indicates that, theoretically, the  $\beta'$ -As<sub>2</sub>Te<sub>3</sub> phase in  $P2_1/m$  should be unstable at 0 K. In fact, as explained in our prior study,<sup>29</sup> starting with the initial parameters of the  $P2_1/m$  space group, the DFT relaxation converges to the loss of the modulation along the  $b$  axis and hence, to a description of the crystal structure in the space group  $C2/m$ , stable at 0 K as shown in Fig. 3a. Although these DFT calculations suggest a higher symmetry at 0 K, we emphasize that the  $\beta'$ -As<sub>2</sub>Te<sub>3</sub> in  $P2_1/m$  is likely stabilized by the phonon contribution at finite temperatures. In order to compare with specific heat measurements, the thermodynamic

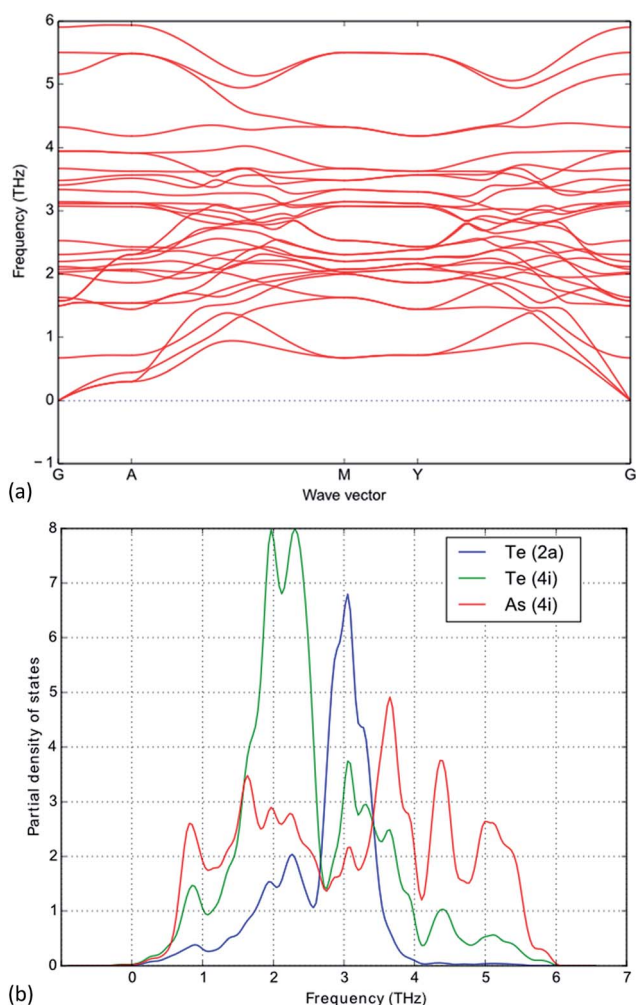


Fig. 3 (a) Phonon dispersion curves and (b) partial phonon DOS of the  $\beta$ -As<sub>2</sub>Te<sub>3</sub> phase calculated in the irreducible  $C2/m$  Brillouin zone.

properties of  $\beta$ -As<sub>2</sub>Te<sub>3</sub> and  $\beta'$ -As<sub>2</sub>Te<sub>3</sub> were only computed in the space groups  $R\bar{3}m$  and  $C2/m$ , respectively, within the quasi-harmonic approximation.

### Specific heat

Fig. 4a shows the specific heat data  $C_p(T)$  measured down to 2 K together with the theoretical curves  $C_v(T)$  calculated for the  $\beta$  phase whereby we assume  $C_p(T) \approx C_v(T)$ , an hypothesis usually justified at low temperatures in solids. The calculated curve of the  $\beta'$  phase (not shown) is the same as that obtained for the  $\beta$  phase. In general, a good correspondence can be observed between measured and calculated data indicating that the vibrational properties of  $\beta$ -As<sub>2</sub>Te<sub>3</sub> have been satisfactorily captured by the *ab initio* calculations. Fitting the low-temperature data, plotted as  $C_p(T)$  versus  $T^2$  in Fig. 4b, according to the free-electron formula  $C_p(T) = \gamma + \beta T^2$  yields an electronic contribution  $\gamma$  indistinguishable from zero to within experimental uncertainty indicating that the phase transition does not influence the semiconducting nature of  $\beta$ -As<sub>2</sub>Te<sub>3</sub> as predicted by our calculations. The  $\beta$  parameter of the phonon contribution gives a low Debye temperature of 148 K, similar to that observed in other chalcogenides such as Bi<sub>2</sub>Te<sub>3</sub> (160 K) or the polymorph  $\alpha$ -As<sub>2</sub>Te<sub>3</sub> (179 K).<sup>42</sup> This Debye temperature corresponds to a frequency of 3.1 THz, in agreement with the mean phonon energy of the calculated PDOS spectrum (Fig. 3b).

In addition to a monotonously increasing specific heat with increasing temperature as expected from a phonon contribution, the  $\beta$ -to- $\beta'$  phase transition shows up as a pronounced hump between 160 K and 210 K, peaking at 185 K. In agreement with our calculations, the similar specific heat values, below and above the transition, indicate nearly identical vibrational spectra due to the close relation between the crystal structures of the  $\beta$  and  $\beta'$  phases. The relaxation curve, monitored across the transition (not shown) does not exhibit signs of shoulders, which would be direct evidence for a thermal arrest in

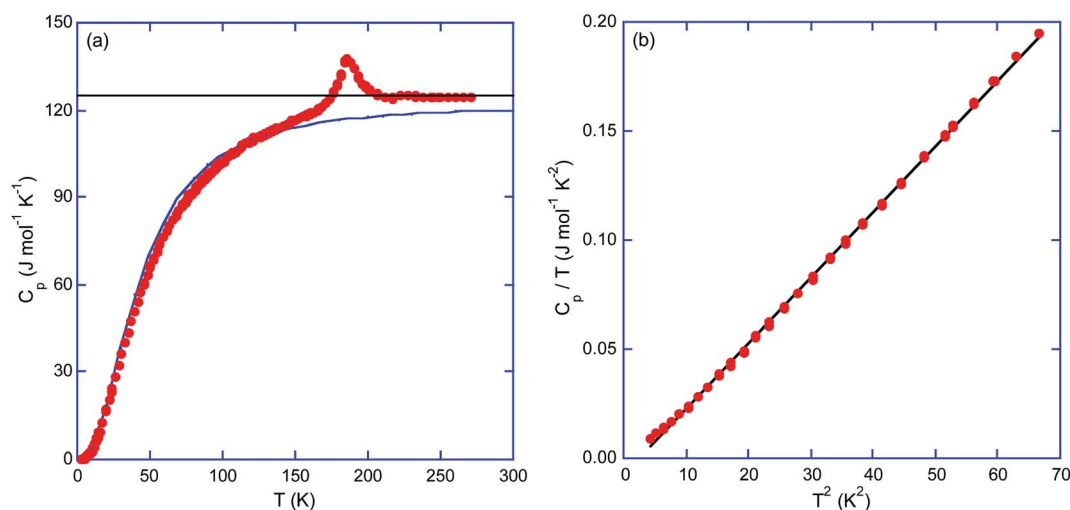


Fig. 4 (a) Specific heat as a function of temperature of  $\beta$ -As<sub>2</sub>Te<sub>3</sub> (red filled circle).  $C_p$  obtained by QHA phonon calculations is represented by the solid blue curve. The horizontal black solid line stands for the Dulong–Petit limit of  $3NR$  where  $N$  is the number of atoms per formula unit and  $R$  is the gas constant. (b) Low-temperature specific heat data plotted as  $C_p/T$  versus  $T^2$ . The solid black line is the best fit to the data according to the free-electron formula  $C_p/T = \gamma + \beta T^2$ .

agreement with the first-order nature of the phase transition. This is another consequence of the small crystallographic differences existing between both phases. The latent heat  $\Delta H$  and entropy  $\Delta S$  were calculated by integrating the  $C_p(T)$  and  $C_p(T)/T$  data, respectively, leading to respective values of  $\sim 323 \text{ J mol}^{-1} \text{ K}^{-1}$  and  $1.3 \text{ J mol}^{-1} \text{ K}^{-2}$ , the latter being consistent with that estimated from differential scanning calorimetry measurements.<sup>29</sup>

### Transport properties

The electrical resistivity measured in the parallel and perpendicular directions as a function of the temperature is shown in Fig. 5a. The measured values are low and indicative of a metallic-like electrical conduction. This first result contrasts with our DFT calculations predicting a semiconducting ground state of the  $\beta$  phase. In the  $(\text{Bi,Sb})_2\text{X}_3$ -based alloys ( $\text{X} = \text{Se, Te}$ ), defect chemistry is known to play a decisive role on the

electronic transport properties, heavily-doped n- or p-type behaviors being achievable in bulk specimens depending on the synthesis conditions.<sup>2</sup> In  $\text{Bi}_2\text{Te}_3$  for instance, both antisite defects ( $\text{Bi}_{\text{Te}}$  and  $\text{Te}_{\text{Bi}}$ ) and vacancies on the Bi or Te sites are electrically active.<sup>43</sup> While  $\text{Bi}_{\text{Te}}$  defects and Bi vacancies act as hole dopants,  $\text{Te}_{\text{Bi}}$  and Te vacancies behave as electron donors. Thus, the p-type metallic properties observed suggest that the present sample is heavily doped by acceptors and hint at the presence of  $\text{As}_{\text{Te}}$  antisite defects and/or As vacancies. The fact that this compound is also prone to variations in the antisite defects and/or vacancy concentration may naturally explain the slight differences observed between the present values and those reported in our prior study.<sup>28</sup>

Upon cooling,  $\rho(T)$  decreases from 300 to 200 K where a steplike increase is observed with a visible hysteresis between the cooling and heating data in the parallel direction. The  $-\text{d}\rho/\text{d}T$  data (Fig. 5b) evidence that the transition extends between

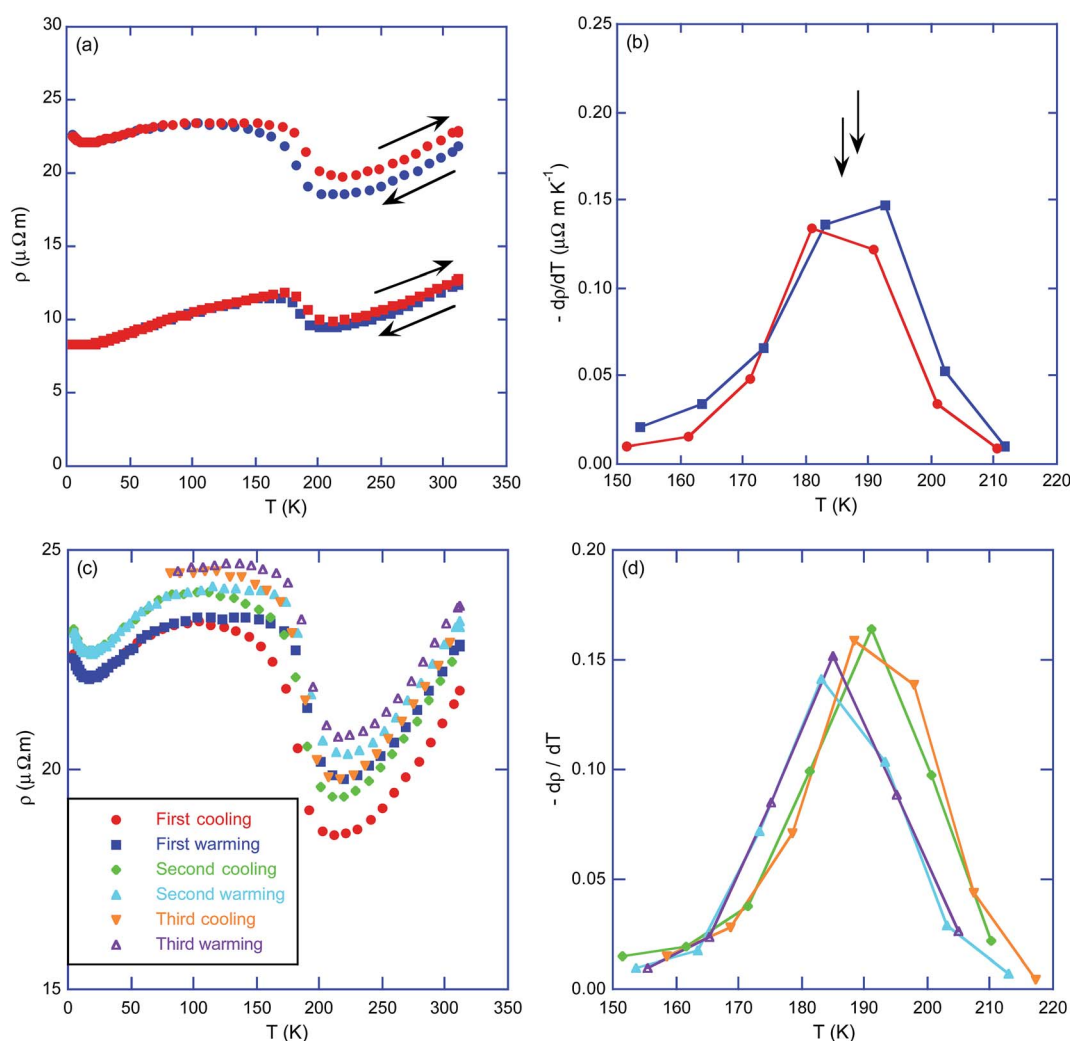


**Fig. 5** (a) Temperature dependence of the electrical resistivity measured during cooling (in blue) and heating (in red) on the samples cut parallel (circle symbol) and perpendicular (square symbol) to the pressing direction. (b)  $-\text{d}\rho/\text{d}T$  as a function of temperature for cooling and warming runs in the parallel direction. The solid lines are guides to the eye. The black vertical arrows indicate the position of the maxima used to estimate the extension of the thermal hysteresis. (c) Electrical resistivity data measured in the parallel direction over three cycles. (d) First-derivative of the electrical resistivity data shown in panel (c). The solid lines are guides to the eye. The color-coded symbols are similar to those indicated in panel (c).

210 K and 160 K with maxima at 186 and 188 K for the cooling and heating runs, respectively. This anomaly is consistent with the first-order phase transition revealed in our prior study.<sup>29</sup>  $\rho(T)$  remains nearly constant from 160 K down to 2 K with a shallow minimum visible near 15 K in the parallel direction while in the perpendicular direction,  $\rho(T)$  smoothly decreases down to 25 K where it tends to level off. Upon warming, the  $\rho$  values measured in the parallel direction are higher than those taken during cooling with no sign of merging up to 300 K. This effect is however less discernable in the perpendicular direction to within experimental uncertainty. Similar behaviors have already been observed in other systems such as in  $\text{Gd}_5(\text{Si/Ge})_4$  where a first-order martensitic transition develops between 250 and 300 K.<sup>44</sup> The slight difference in  $\rho(T)$  during the thermal cycle had not only been attributed to the transition itself but also to microcracks in the sample volume that form in the course of the transformation. Although the present transition does not show a martensitic character, internal stresses that appear during the transition may be responsible for the observed increase in  $\rho$ . This possibility seems corroborated by the data collected over three thermal cycles on the sample cut parallel to the pressing direction. As shown in Fig. 5c, a systematic change in the electrical resistivity ratio  $\rho_{300\text{K}}/\rho_{5\text{K}}$  is observed during cycles. The 2 K hysteresis observed during the first cycle remains nearly unchanged during the following cycles (Fig. 5d).

Measurement of the Hall coefficient reveals a dominant hole-like signal in the whole temperature range in agreement with our electronic band structure calculations. While the  $p$ -type character of  $\beta\text{-As}_2\text{Te}_3$  remains unaffected across the transition, the changeover to the  $\beta'$  phase is clearly visible as a pronounced minimum (Fig. 6). Likewise  $\alpha\text{-As}_2\text{Te}_3$  (ref. 42), the anisotropic crystal structure of  $\beta\text{-As}_2\text{Te}_3$  results in a galvanomagnetic tensor with several independent components.<sup>45</sup> This property could in principle give rise to distinct Hall coefficients in the parallel and

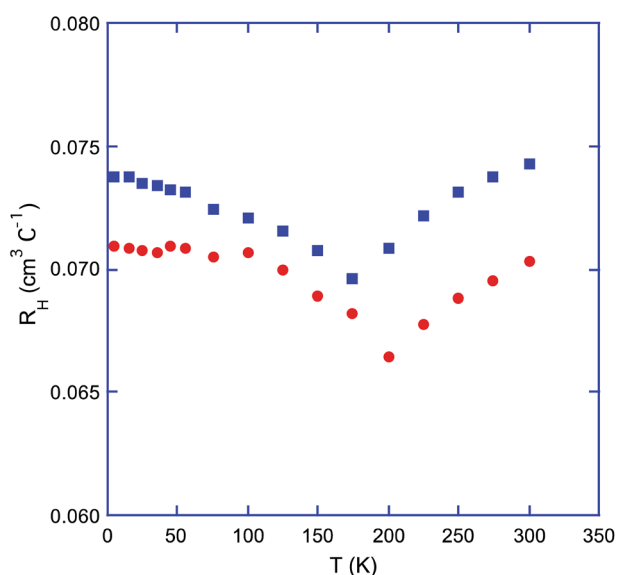


Fig. 6 Hall coefficient  $R_H$  as a function of the temperature measured parallel (●) and perpendicular (■) to the pressing direction.

perpendicular directions. However, in the present case, the anisotropy in the  $R_H$  values amounts to at most 6% at 300 K, which is at the border of the experimental uncertainty. The Hall hole concentration  $p$  can be thus estimated to a good approximation with a single-carrier relation. The  $R_H$  value yields an estimated  $p$  value of  $9 \times 10^{19} \text{ cm}^{-3}$  at 300 K, which shows only little variations with temperature consistent with the idea that  $\beta\text{-As}_2\text{Te}_3$  is intrinsically heavily-doped.

In agreement with the sign of the Hall coefficient, the thermopower (Fig. 7) is positive, indicative of holes as the dominant charge carriers. This result differs from that obtained by Scheidemantel *et al.*<sup>41</sup> who measured negative thermopower values. However, this discrepancy is likely explained by the fact that their measurement was done under different conditions *i.e.* by subjecting  $\alpha\text{-As}_2\text{Te}_3$  to high pressures up to 10 GPa, the  $\alpha$  phase transforming into the  $\beta$  phase at 8 GPa.<sup>41</sup> As shown in Fig. 7,  $\alpha$  varies linearly with temperature as typically observed in nonmagnetic metals and heavily-doped semiconductors. The transition is visible between 170 and 190 K as a small jump in the  $\alpha$  values. Within experimental uncertainty, no difference between the data taken on cooling and heating is observed nor between the data measured in the parallel or in the perpendicular directions. This conclusion holds true regardless of the number of cycles performed (not shown) indicating that the hysteresis is too weak to be clearly observable in the  $\alpha(T)$  data. This observation is consistent with the low-temperature X-ray and neutron diffraction experiments revealing that only subtle differences exist between the  $\beta$  and  $\beta'$  phases.<sup>29</sup> Because the thermopower is sensitive to changes in the electronic band structure near the chemical potential, these results are also consistent with our first-principles calculations indicating that

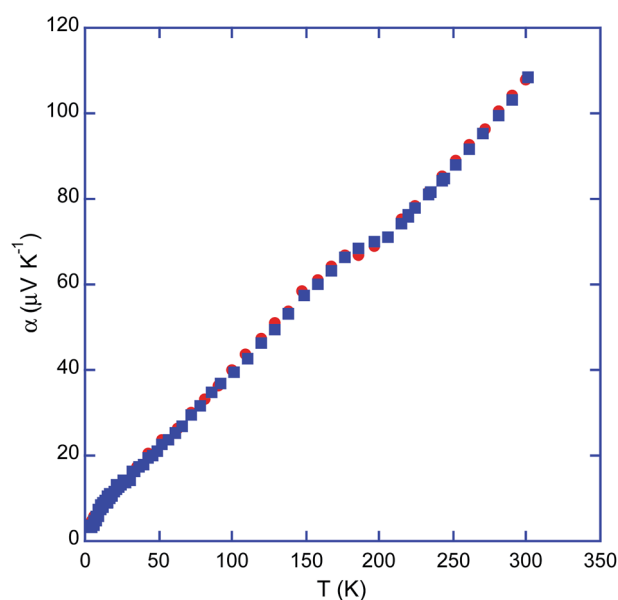


Fig. 7 Thermopower as a function of temperature of  $\beta\text{-As}_2\text{Te}_3$ . For sake of clarity, only the data collected in the parallel direction are shown. Measurement in the perpendicular direction yielded similar values and temperature dependences to within experimental uncertainty.

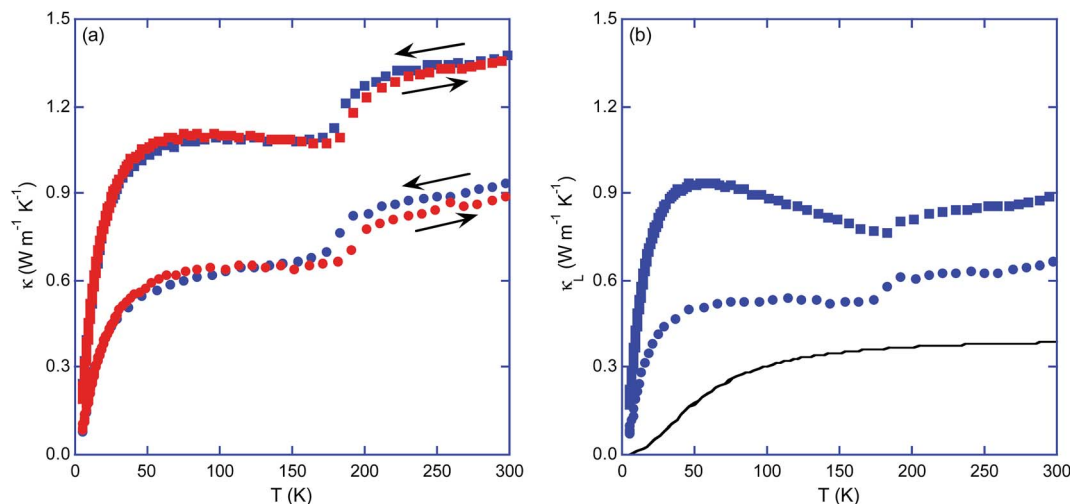


Fig. 8 (a) Temperature dependence of the total thermal conductivity of  $\beta$ -As<sub>2</sub>Te<sub>3</sub> measured parallel (circle symbol) and perpendicular (square symbol) to the pressing direction for cooling (in blue) and heating (in red) runs as indicated by the black arrows. (b) Lattice thermal conductivity as a function of temperature for the data collected upon cooling parallel (circle symbol) and perpendicular (square symbol) to the pressing direction. The black solid curve stands for the minimum lattice thermal conductivity estimated by the model developed by Cahill and Pohl.<sup>49,50</sup>

the phase transition has little influence on the overall electronic properties of  $\beta$ -As<sub>2</sub>Te<sub>3</sub>.

As shown in Fig. 8a, the thermal conductivity is also influenced by the first-order transition. Noteworthy, the absence of dielectric maximum at low temperatures, featuring the “glass-like behavior” of  $\kappa$ , might be ascribed to the distorted structure of  $\beta'$  alone (which might not be the case for the  $\beta$  phase, should it be stable below 180 K). The  $\kappa$  values, nearly constant between 200 and 300 K ( $0.8 \text{ W m}^{-1} \text{ K}^{-1}$ ), drop significantly below 200 K to  $0.6 \text{ W m}^{-1} \text{ K}^{-1}$ . The difference between the cooling and heating data at 300 K reflects almost entirely the difference observed in the  $\rho$  values that impact the electronic contribution  $\kappa_e$  to  $\kappa$ . This contribution was estimated using the Wiedemann–Franz relation  $\kappa_e = LT/\rho$  where  $L$  is the Lorenz number. As a first approximation, we used a single-parabolic band model assuming acoustic phonon scattering as the main mechanism of charge carrier diffusion to estimate the Lorenz number. This approach was extended down to 5 K to determine the temperature dependence of  $L$  that exhibits a room-temperature value of  $1.9 \times 10^{-8} \text{ V}^2 \text{ K}^{-2}$  and tends to the degenerate value of  $2.45 \times 10^{-8} \text{ V}^2 \text{ K}^{-2}$  in the limit  $T \rightarrow 0 \text{ K}$ . The resulting temperature dependence of the lattice thermal conductivity  $\kappa_L = \kappa - \kappa_e$  is shown in Fig. 8b. For sake of clarity, only the  $\kappa_L$  values estimated from the data taken upon cooling are shown, the values upon heating being nearly identical. The  $\kappa_L$  values are extremely low reaching 0.8 and  $0.6 \text{ W m}^{-1} \text{ K}^{-1}$  at 300 K in the perpendicular and parallel directions, respectively. The  $\beta$ -to- $\beta'$  transition only weakly impacts the  $\kappa_L$  values in agreement with the trend previously revealed by the calculations of the phonon properties. These values are even lower than those measured in the Bi<sub>2</sub>Te<sub>3</sub> analogues but are similar to those achieved in monoclinic  $\alpha$ -As<sub>2</sub>Te<sub>3</sub> and in several other chalcogenides such as SnSe or In<sub>4</sub>Se<sub>3</sub>.<sup>16,46–50</sup> There is a large body of evidence indicating that the lattice thermal conductivity roughly scales inversely with the unit cell size, large unit cells

favoring very low  $\kappa_L$  values. However, this general guideline breaks down in the present case, the simple crystal structure of  $\beta$ -As<sub>2</sub>Te<sub>3</sub> suggesting the presence of an efficient phonon scattering mechanism in this material. To estimate the minimum lattice thermal conductivity  $\kappa_{\text{min}}$  and hence, to determine whether or not further reduction may be achieved, we used the formula derived by Cahill *et al.*<sup>51,52</sup> for disordered crystals.  $\kappa_{\text{min}}$  depends on the longitudinal and transverse sound velocities  $v_l$  and  $v_t$ , respectively. Using the values derived in ref. 38 ( $v_l = 3953 \text{ m s}^{-1}$  and  $v_t = 2357 \text{ m s}^{-1}$ ), this approach yields  $\kappa_{\text{min}} \approx 0.4 \text{ W m}^{-1} \text{ K}^{-1}$  at 300 K (Fig. 8b). Near this temperature, the lattice thermal conductivity of  $\beta$ -As<sub>2</sub>Te<sub>3</sub> approaches  $\kappa_{\text{min}}$  in the parallel direction suggesting only little room for further optimization.

## Conclusion

In this study, we reported a detailed investigation of the low-temperature transport and thermodynamic properties of  $\beta$ -As<sub>2</sub>Te<sub>3</sub>, complemented by density functional theory calculations of both electronic and vibrational properties of the  $\beta$  and  $\beta'$  phases. DFT calculations showed that the first-order lattice distortion undergone near 190 K has little influence on the semiconducting ground state and on the thermal transport as observed experimentally. Measurements of the electrical resistivity upon cooling and heating across the lattice distortion revealed a hysteretic behavior, perhaps due to internal stresses. Finally, the very low sound velocities and the fact that the acoustic phonon branches are limited to a narrow energy window evidenced by our calculations explain the low lattice thermal conductivities measured in  $\beta$ -As<sub>2</sub>Te<sub>3</sub>.

## Acknowledgements

The authors acknowledge the financial support from the French National Agency (ANR) in the frame of its program

“PROGELEC” (Verre Thermo-Générateur “VTG”). DFT and phonon calculations were performed using HPC resources from GENCI - CINES (Grant 2015-096175).

## References

- H. J. Goldsmid, in *Thermoelectric Refrigeration*, Temple Press Books Ltd, London, U.K., 1964.
- Thermoelectrics and Its Energy Harvesting*, ed. D. M. Rowe, CRC Press, Boca Raton, FL, 2012.
- S. M. Kauzlarich, S. R. Brown and G. J. Snyder, *Dalton Trans.*, 2007, 2099–2107.
- E. S. Toberer, A. Zevalkink, N. Crisosto and G. J. Snyder, *Adv. Funct. Mater.*, 2010, **20**, 4375.
- S. K. Bux, A. Zevalkink, O. Janka, D. Uhl, S. Kauzlarich, J. G. Snyder and J.-P. Fleurial, *J. Mater. Chem. A*, 2014, **2**, 215.
- U. Aydemir, A. Zevalkink, A. Ormeci, Z. M. Gibbs, S. Bux and G. J. Snyder, *Chem. Mater.*, 2015, **27**, 1622.
- S. R. Brown, S. M. Kauzlarich, F. Gascoin and G. J. Snyder, *Chem. Mater.*, 2006, **18**, 1873.
- T. Zhou, B. Lenoir, M. Colin, A. Dauscher, R. Al Rahal Al Orabi, P. Gougeon, M. Potel and E. Guilmeau, *Appl. Phys. Lett.*, 2011, **98**, 162106.
- R. Al Rahal Al Orabi, P. Gougeon, P. Gall, B. Fontaine, R. Gautier, M. Colin, C. Candolfi, A. Dauscher, J. Hejtmanek, B. Malaman and B. Lenoir, *Inorg. Chem.*, 2014, **53**, 11699.
- T. Zhou, M. Colin, C. Candolfi, C. Boulanger, A. Dauscher, E. Santava, J. Hejtmanek, P. Baranek, R. Al Rahal Al Orabi, M. Potel, B. Fontaine, P. Gougeon, R. Gautier and B. Lenoir, *Chem. Mater.*, 2014, **26**, 4765.
- H. Wang, E. Schechtel, Y. Pei and G. J. Snyder, *Adv. Energy Mater.*, 2013, **3**, 488.
- Q. Zhang, E. Kebede Chere, J. Sun, F. Cao, K. Dahal, S. Chen, G. Chen and Z. Ren, *Adv. Energy Mater.*, 2015, **5**, 1500360.
- Q. Tan, L.-D. Zhao, J.-F. Li, C.-F. Wu, T.-R. Wei, Z.-B. Xing and M. G. Kanatzidis, *J. Mater. Chem. A*, 2014, **2**, 17302.
- A. Banik and K. Biswas, *J. Mater. Chem. A*, 2014, **2**, 9620.
- Y. Chen, M. D. Nielsen, Y.-B. Gao, T.-J. Zhu, X. Zhao and J. P. Heremans, *Adv. Energy Mater.*, 2012, **2**, 58.
- S. Sassi, C. Candolfi, J.-B. Vaney, V. Ohorodniichuk, P. Masschelein, A. Dauscher and B. Lenoir, *Appl. Phys. Lett.*, 2014, **104**, 212105.
- K. Suekuni, K. Tsuruta, T. Ariga and M. Koyano, *Appl. Phys. Express*, 2012, **5**, 051201.
- X. Lu, D. T. Morelli, Y. Xia, F. Zhou, V. Ozolins, H. Chi, X. Zhou and C. Uher, *Adv. Energy Mater.*, 2013, **3**, 342.
- K. Suekuni, F. S. Kim, H. Nishiate, M. Ohta, H. I. Tanaka and T. Takabatake, *Appl. Phys. Lett.*, 2014, **105**, 132107.
- P. Qiu, T. Zhang, Y. Qiu, X. Shi and L. Chen, *Energy Environ. Sci.*, 2014, **7**, 4000.
- Y. Bouyrie, C. Candolfi, S. Pailhès, M. M. Koza, B. Malaman, A. Dauscher, J. Tobola, O. Boisron, L. Saviot and B. Lenoir, *Phys. Chem. Chem. Phys.*, 2015, **17**, 19751.
- Y. Bouyrie, C. Candolfi, V. Ohorodniichuk, B. Malaman, A. Dauscher, J. Tobola and B. Lenoir, *J. Mater. Chem. C*, 2015, **3**, 10476.
- Y. S. Hor, P. Roushan, H. Beidenkopf, J. Seo, D. Qu, J. G. Checkelsky, L. A. Wray, D. Hsieh, Y. Xia, S.-Y. Xu, D. Qian, M. Z. Hasan, N. P. Ong, A. Yazdani and R. J. Cava, *Phys. Rev. B: Condens. Matter*, 2010, **81**, 195203.
- Y. S. Hor, A. Richardella, P. Roushan, Y. Xia, J. G. Checkelsky, A. Yazdani, M. Z. Hasan, N. P. Ong and R. J. Cava, *Phys. Rev. B: Condens. Matter*, 2009, **79**, 195208.
- H. Zhang, C.-X. Liu, X.-L. Qi, X. Dai, Z. Fang and S.-C. Zhang, *Nat. Phys.*, 2009, **5**, 438.
- Y. Xia, D. Qian, D. Hsieh, L. A. Wray, A. Pal, H. Lin, A. Bansil, D. Grauer, Y. S. Hor and R. J. Cava, *Nat. Phys.*, 2009, **5**, 398.
- Y. S. Hor, J. G. Checkelsky, P. Roushan, J. Seo, Q. Xu, H. W. Zandbergen, A. Yazdani, N. P. Ong and R. J. Cava, *Phys. Rev. Lett.*, 2010, **104**, 057001.
- J. B. Vaney, J. Carreaud, G. Delaizir, A. Pradel, A. Piarristeguy, C. Morin, E. Alleno, J. Monnier, A. P. Goncalves, C. Candolfi, A. Dauscher and B. Lenoir, *Adv. Electron. Mater.*, 2015, **1**, 1400008.
- C. Morin, S. Corallini, J. Carreaud, J. B. Vaney, G. Delaizir, J.-C. Crivello, E. B. Lopes, A. Piarristeguy, J. Monnier, C. Candolfi, V. Nassif, G. Cuello, A. Pradel, A. P. Goncalves, B. Lenoir and E. Alleno, *Inorg. Chem.*, 2015, **54**, 9936.
- P. E. Blöchl, *Phys. Rev. B: Condens. Matter*, 1994, **50**, 17953.
- G. Kresse and J. Hafner, *Phys. Rev. B: Condens. Matter*, 1993, **47**, 558.
- G. Kresse and J. Furthmüller, *Phys. Rev. B: Condens. Matter*, 1996, **54**, 11169.
- J. P. Perdew, K. Burke and M. Ernzerhof, *Phys. Rev. Lett.*, 1997, **78**, 1396.
- L. Chaput, A. Togo, I. Tanaka and G. Hug, *Phys. Rev. B: Condens. Matter*, 2011, **84**, 094302.
- K. Parlinski, Z. Q. Li and Y. Kawazoe, *Phys. Rev. Lett.*, 1997, **78**, 4063.
- A. Togo, F. Oba and I. Tanaka, *Phys. Rev. B: Condens. Matter*, 2008, **78**, 134106.
- T. Scheidemantel and J. Badding, *Solid State Commun.*, 2003, **127**, 667.
- H. Deng, *J. Alloys Compd.*, 2016, **656**, 695.
- K. Pal and U. V. Waghmare, *Appl. Phys. Lett.*, 2014, **105**, 062105.
- Y. Sharma and P. Srivastava, *Opt. Mater.*, 2011, **33**, 899.
- T. J. Scheidemantel, J. F. Meng and J. V. Badding, *J. Phys. Chem. Solids*, 2005, **66**, 1744.
- J.-B. Vaney, J. Carreaud, G. Delaizir, A. Piarristeguy, A. Pradel, E. Alleno, J. Monnier, E. B. Lopes, A. P. Goncalves, A. Dauscher, C. Candolfi and B. Lenoir, *J. Mater. Chem. C*, 2016, **4**, 2329–2338.
- P. Pecheur and G. Toussaint, *J. Phys. Chem. Solids*, 1994, **55**, 327–338.
- E. M. Levin, O. Pecharsky, V. K. Pecharsky and K. A. Gschneidner, *Phys. Rev. B: Condens. Matter*, 2001, **63**, 064426.
- Y. C. Akgöz and G. A. Saunders, *J. Phys. C: Solid State Phys.*, 1975, **8**, 1387–1396.
- C.-L. Chen, H. Wang, Y.-Y. Chen, T. Day and G. J. Snyder, *J. Mater. Chem. A*, 2014, **2**, 11171.

- 47 Q. Zhang, E. Kedebe Chere, J. Sun, F. Cao, K. Dahal, S. Chen, G. Chen and Z. Ren, *Adv. Energy Mater.*, 2015, **5**, 1500360.
- 48 J.-S. Rhyee, K. H. Lee, S. M. Lee, E. Cho, S. Kim, E. Lee, Y. S. Kwon, J. H. Shim and G. Kotliar, *Nature*, 2009, **459**, 965.
- 49 J. H. Kim, M. J. Kim, S. Oh, J.-S. Rhyee, S.-D. Park and D. Ahn, *Dalton Trans.*, 2015, **44**, 3185.
- 50 Z.-S. Lin, L. Chen, L.-M. Wang, J.-T. Zhao and L.-M. Wu, *Adv. Energy Mater.*, 2013, **25**, 4800.
- 51 D. G. Cahill, S. K. Watson and R. O. Pohl, *Phys. Rev. B: Condens. Matter*, 1992, **46**, 6131.
- 52 D. G. Cahill and R. O. Pohl, *Annu. Rev. Phys. Chem.*, 1988, **39**, 93.